THE 21 cm BACKGROUND FROM THE COSMIC DARK AGES: MINIHALOS AND THE INTERGALACTIC MEDIUM BEFORE REIONIZATION

PAUL R. SHAPIRO,[1] KYUNGJIN AHN,[1] MARCELO A. ALVAREZ,[1]
ILIAN T. ILIEV,[2] HUGO MARTEL,[3] AND DONGSU RYU[4]

ABSTRACT

The H atoms inside minihalos (i.e., halos with virial temperatures $T_{vir} \leq 10^4$ K, in the mass range roughly from 10^4 to $10^8\ M_\odot$) during the cosmic dark ages in a ΛCDM universe produce a redshifted background of collisionally pumped 21 cm line radiation that can be seen in emission relative to the cosmic microwave background (CMB). Previously, we used semianalytical calculations of the 21 cm signal from individual halos of different mass and redshift and the evolving mass function of minihalos to predict the mean brightness temperature of this 21 cm background and its angular fluctuations. Here we use high-resolution cosmological N-body and hydrodynamic simulations of structure formation at high redshift ($z \gtrsim 8$) to compute the mean brightness temperature of this background from both minihalos and the intergalactic medium (IGM) prior to the onset of Lyα radiative pumping. We find that the 21 cm signal from gas in collapsed, virialized minihalos dominates over that from the diffuse shocked gas in the IGM.

Subject headings: cosmology: theory — diffuse radiation — galaxies: formation — intergalactic medium — large-scale structure of universe — radio lines: galaxies

1. INTRODUCTION

One of the most promising means by which to observe the high-redshift universe in the cosmic "dark ages" is through the 21 cm wavelength hyperfine transition of the neutral hydrogen that is abundant prior to reionization (e.g., Scott & Rees 1990; Subramanian & Padmanabhan 1993). Motivated by the prospect of new radio telescopes that will be able to observe such a signal, several specific observational techniques have been proposed. Among these are the angular fluctuations on the sky (e.g., Madau et al. 1997; Tozzi et al. 2000; Iliev et al. 2002 [hereafter ISFM02], 2003; Ciardi & Madau 2003; Zaldarriaga et al. 2004; Furlanetto et al. 2004), features in the frequency spectrum of the signal averaged over a substantial patch of the sky (Shaver et al. 1999; Gnedin & Shaver 2004) and studies of absorption features in the spectra of bright, high-redshift radio sources (Carilli et al. 2002; Furlanetto & Loeb 2002; Martel et al. 2003).

For most of these techniques, with the exception of foreground absorption against bright radio sources, the 21 cm signal must be distinguished from the CMB, which is only possible if the 21 cm level population corresponds to a spin temperature T_S, which differs from the temperature, T_{CMB}, of the CMB. Since radiative excitation and stimulated emission of this transition by CMB photons tends to drive the value of T_S toward T_{CMB}, some competing mechanism must exist to decouple T_S from T_{CMB}. There are two main physical mechanisms by which the spin temperature is decoupled from the CMB temperature: "Lyα pumping," or absorption of radiation with a wavelength in the Lyα transition, followed by decay into one of the hyperfine levels of the ground state (the "Field-Wouthuysen effect"; Wouthuysen

1952; Field 1959), and spin exchange during collisions between neutral hydrogen atoms (Purcell & Field 1956). The efficiency of Lyα pumping depends on the intensity of the UV radiation field at the Lyα transition, whereas the efficiency of collisional coupling depends on the local gas density and temperature.

For $z \gtrsim 150$, these mechanisms are ineffective at decoupling T_S from T_{CMB}, since the kinetic temperature of the gas, T_K, is coupled to T_{CMB} by inverse Compton scattering, and sources of UV radiation have not yet formed to initiate Lyα pumping. At $z \lesssim 150$, however, T_K drops below T_{CMB} and, for $z \gtrsim 20$, gas at the mean density is sufficiently dense for collisions to couple T_S to T_K. During the dark ages, therefore, when there is no Lyα pumping, the mean 21 cm signal against the CMB will be zero at $z \gtrsim 150$, then in absorption at $20 \lesssim z \lesssim 150$.

At lower redshift, collisions become negligible for gas at or below the cosmic mean density, and such gas becomes invisible until its spin temperature is again decoupled from the CMB by Lyα pumping due to an early UV background from the first stars and quasars. Even though collisional decoupling is ineffective for $z \lesssim 20$ for gas at the *mean* density, gas in overdense and/or heated regions can still be collisionally decoupled. In particular, the gas density within "minihalos"—virialized halos of dark and baryonic matter with masses $10^4\ M_\odot \lesssim M \lesssim 10^8\ M_\odot$ and virial temperatures $T < 10^4$ K that are too low to collisionally ionize their H atoms—is sufficiently high so as to decouple its gas spin temperature from the CMB, with $T_S > T_{CMB}$ in general, causing it to appear in emission (ISFM02). ISFM02 predicted the mean and angular fluctuations of the corresponding 21 cm signal by a semianalytical calculation that integrated the equation of transfer through individual minihalos of different mass at different redshifts ($z > 6$) and summed these individual halo contributions over the evolving statistical distribution of minihalo masses in the ΛCDM universe. Iliev et al. (2003) extended these results to include nonlinear biasing effects. These authors concluded that the fluctuations in intensity across the sky created by minihalos were likely to be observable by the next generation of low-frequency radio telescopes. Such observations could confirm the basic CDM paradigm and constrain the shape and

[1] Department of Astronomy, University of Texas at Austin, 1 University Station, C1400, Austin, TX 78712.
[2] Canadian Institute for Theoretical Astrophysics, University of Toronto, 60 St. George Street, Toronto, ON M5S 3H8, Canada.
[3] Département de Physique, de Génie Physique et d'Optique, Université Laval, Québec, QC G1K 7P4, Canada.
[4] Department of Astronomy and Space Science, Chungnam National University, Daejeon 305-764, South Korea.

amplitude of the power spectrum at much smaller scales than previously possible.

Since then, Furlanetto & Loeb (2004) have suggested that shocked, overdense gas in the diffuse IGM (prior to the onset of Lyα radiative pumping) is also capable of producing a 21 cm emission signal and that this IGM contribution to the mean signal will dominate over that from gas inside minihalos. Their conclusion is based on an extension of the Press-Schechter approximation (Press & Schechter 1974) that is used to determine the fraction of baryons in the diffuse IGM that are hot and dense enough to produce a 21 cm emission signal. We address this question here.

In order to quantify these effects, we have computed the 21 cm signal both from minihalos and the IGM at $z \gtrsim 8$ for the first time using high-resolution cosmological N-body and hydrodynamic simulations of structure formation. We have assumed a flat ΛCDM cosmology with matter density parameter $\Omega_m = 0.27$, cosmological constant $\Omega_\Lambda = 0.73$, baryon density $\Omega_b = 0.043$, Hubble constant $H = 70$ km s^{-1} Mpc^{-1}, linearly extrapolated $\sigma_{8\,h^{-1}} = 0.9$, and the "untilted" Harrison-Zel'dovich primordial power spectrum.

In this paper, we present detailed, high-resolution gas and N-body simulations that predict the 21 cm signal at $z > 6$ due to collisional decoupling from the CMB before the UV background is strong enough to make decoupling due to Lyα pumping important. Because the Lyα pumping efficiency is expected to fluctuate strongly until enough sources form to make the efficiency uniform (e.g., Barkana & Loeb 2004), the results presented here will also be relevant for isolated patches of the universe during reionization itself, which would depend on the location and abundance of the first sources of UV radiation. Within such regions, we focus on properly resolving the gasdynamics of structure formation at small scales through the use of high-resolution gasdynamic and N-body simulations. We test the semianalytical prediction of the halo model of ISFM02 for the contribution to the mean signal from gas in minihalos and investigate the extent to which IGM gas may provide a nonnegligible contribution to the total fluctuating signal, as suggested by Furlanetto & Loeb (2004).

These results were first summarized in Ahn et al. (2006). Here we describe our calculations in full and present our results in more detail.

The outline of this paper is as follows. In § 2 we summarize the basic physics of the 21 cm emission and absorption and the analytical model of ISFM02. We also describe our cosmological simulations and their initial conditions, and our method for obtaining the 21 cm signal from our simulations. In § 3 we present our results. Our conclusions are summarized in § 4.

2. THE CALCULATION

2.1. *Physics of* 21 cm *Signal from Neutral Hydrogen*

The hyperfine splitting of the ground state of hydrogen leads to a transition with excitation temperature $T_* = 0.068$ K, wavelength $\lambda_0 = 21.16$ cm, and frequency $\nu_0 = 1.417$ GHz. The ratio of populations of the upper (n_1) and lower (n_0) states is characterized by the spin temperature T_S according to

$$\frac{n_1}{n_0} = 3 \exp\left(-\frac{T_*}{T_S}\right). \tag{1}$$

Neutral hydrogen at redshift z produces a differential signal relative to the CMB at redshifted wavelength $21(1 + z)$ cm only if T_S differs from $T_{\rm CMB}$. The 21 cm transition is seen in emission

against the CMB if $T_S > T_{\rm CMB}$, or in absorption if $T_S < T_{\rm CMB}$. The value of T_S is determined by the relative importance of collisional and radiative excitations. A hydrogen atom can (1) absorb a 21 cm photon from the CMB (CMB pumping), (2) collide with another atom (collisional pumping), and (3) absorb a Lyα photon to make a Lyα transition, then decay to one of the hyperfine 21 cm levels (Lyα pumping). These pumping mechanisms jointly determine the spin temperature,

$$T_S = \frac{T_{\rm CMB} + y_\alpha T_\alpha + y_c T_K}{1 + y_\alpha + y_c}, \tag{2}$$

where T_α is the color temperature of the Lyα photons, T_K is the kinetic temperature, y_α is the Lyα coupling constant, and y_c is the collisional coupling constant (Purcell & Field 1956; Field 1959). As seen in equation (2), the spin temperature deviates from $T_{\rm CMB}$ only when these couplings exist. Throughout this paper, we consider only the collisionally coupled gas, or the case in which $y_\alpha = 0$. This is valid when (1) light sources were not yet abundant enough to build up substantial Lyα background or (2) the region of interest is far enough away from light sources. The collisional coupling constant is given by

$$y_c = \frac{T_* C_{10}}{T_K A_{10}}, \tag{3}$$

where $A_{10} = 2.85 \times 10^{-15}$ s^{-1} is the Einstein spontaneous emission coefficient, and $C_{10} = \kappa(1 - 0)n_{\rm H}$ is the atom-atom collisional de-excitation rate (Purcell & Field 1956). We use $\kappa(1 - 0)$ tabulated in Zygelman (2005), which is valid for 1 K $< T_K < 300$ K, and for higher T_K we use $\kappa(1 - 0)$ tabulated in Allison & Dalgarno (1969).[5]

The 21 cm line can be observed in either absorption or emission against the CMB, with a differential brightness temperature defined by

$$\delta T_b(\nu) \equiv T_b(\nu) - T_{{\rm CMB},\,0}, \tag{4}$$

where $T_b(\nu)$ is the brightness temperature at an observed frequency ν and $T_{\rm CMB,0}$ is the present-day CMB temperature; $T_b(\nu)$ satisfies the radiative transfer equation in the Rayleigh-Jeans limit,

$$T_b(\nu) = T_{{\rm CMB},\,0}e^{-\tau_\nu} + \int_0^{\tau_\nu} d\tau'_{\nu'}\, \frac{T_S(z')}{1 + z'}\, e^{-(\tau_\nu - \tau'_{\nu'})}, \tag{5}$$

where $\tau_\nu = \int_0^{\tau_\nu} d\tau'_{\nu'}$ is the 21 cm optical depth of the neutral hydrogen atoms to photons in the CMB observed today at frequency ν, $\tau'_{\nu'} = \int_0^{\tau'_{\nu'}} d\tau''_{\nu''}$ is the optical depth of the neutral hydrogen atoms at redshift z' to photons at a frequency $\nu' = \nu(1 + z')$ (the frequency that a comoving observer sees at redshift z'), $T_S(z')$ is the spin temperature of intervening gas located at redshift z', and the infinitesimal optical depth along the path of the photon as it travels for cosmic time interval dt' is given by

$$d\tau'_{\nu'} = c\,dt'\kappa_{\nu'}(\nu', z')$$
$$= \left[\frac{c\,dz'}{H(z')(1 + z')}\right]\left[\frac{3c^2 A_{10} n_{\rm H\,I}(z')}{32\pi\nu'^2}\,\phi(\nu')\,\frac{T_*}{T_S(z')}\right], \tag{6}$$

---

[5] The definition of $\kappa(1 - 0)$ in Allison & Dalgarno (1969) is not consistent with that in Zygelman (2005). One should multiply their $\kappa(1 - 0)$ by (4/3) in order to calculate C_{10} when using tabulated $\kappa(1 - 0)$ of Allison & Dalgarno (1969).

where $H(z)$ is the Hubble constant at redshift z, and $n_{\mathrm{H\,I}}$ is the local density of neutral hydrogen. The line profile $\phi(\nu')$ satisfies

$$\int_{-\infty}^{+\infty} d\nu' \phi(\nu') = 1 \qquad (7)$$

and is in a general form. For instance, in the presence of both thermal Doppler broadening and the Doppler shift due to peculiar motion, the line profile is given by

$$\phi(\nu') = \frac{1}{\Delta\nu'\sqrt{\pi}} \exp\left[-\frac{(\nu'-\nu_0')^2}{\Delta\nu'^2}\right], \qquad (8)$$

where $\Delta\nu' = (\nu_0'/c)(2kT/m)^{1/2}$, and the Doppler-shifted line center is given by

$$\nu_0' = \nu_0 \frac{1+\beta}{\sqrt{1-\beta^2}}, \qquad (9)$$

where $\beta = v/c$ is the line-of-sight peculiar velocity of gas (in units of the speed of light) *toward* the observer.

2.1.1. *The Unperturbed Universe*

Solutions to the general radiative transfer equation (eq. [5]) exist in simplified forms in limiting cases. If the line is unbroadened and unshifted, i.e., $\phi(\nu') = \delta(\nu'-\nu_0)$, the solution to equation (5) becomes

$$T_b(\nu) = T_{\mathrm{CMB},0} e^{-\tau(z)} + \frac{T_S(z)}{1+z}\left[1 - e^{-\tau(z)}\right], \qquad (10)$$

where ν and z satisfy $\nu_0 = \nu(1+z)$, and

$$\tau(z) \equiv \frac{3\lambda_0^3 A_{10} T_* n_{\mathrm{H\,I}}(z)}{32\pi T_S H(z)} = 3.22 \times 10^{-3}$$
$$\times \left(\frac{\Omega_b h^2}{0.0224}\right)\left(\frac{\Omega_0 h^2}{0.135}\right)^{-0.5}\left(\frac{T_{\mathrm{CMB}}}{T_S}\right)(1+z)^{0.5}, \quad (11)$$

using $n_{\mathrm{H\,I}} = x_{\mathrm{H\,I}} n_{\mathrm{H}}$, where $n_{\mathrm{H}} = 1.9 \times 10^{-7}\ \mathrm{cm}^{-3}\,(1+z)^3$ and $x_{\mathrm{H\,I}}$ is the neutral fraction of hydrogen. The IGM kinetic temperature, T_K, is coupled to T_{CMB} by Compton scattering at $z \gtrsim 134$. For $z \lesssim 100$, the kinetic temperature of the unperturbed gas in the ΛCDM universe is well approximated by

$$T_K \approx T_{\mathrm{CMB}}(z=134)(1+z)^2/(1+134)^2$$
$$= 368.55\ \mathrm{K}\,(1+z)^2/(1+134)^2. \qquad (12)$$

Since $T_{\mathrm{CMB}}/T_S < \max\{1,\ T_{\mathrm{CMB}}/T_K\}$, in general, $\tau_\nu \ll 1$ for the unperturbed IGM at all redshifts of interest ($8 \lesssim z \lesssim 50$), as seen in equation (11). In that case, equation (10) can be approximated as

$$\delta T_b(\nu) = [T_S(z) - T_{\mathrm{CMB}}(z)]\tau(z)/(1+z) \qquad (13)$$

using equation (4). We can use equations (11) and (13) to describe the signal from the unperturbed gas in the universe, because the line profile in this case is narrow enough to be approximated by a Dirac δ-function. With equations (2), (3), (11), and (13), one can calculate δT_b of the unperturbed gas of the universe, well approximated by

$$\delta T_b(z) \approx -10\ \mathrm{mK}\,\frac{F[\log_{10}(1+z)]}{F[\log_{10}(1+36.8)]}, \qquad (14)$$
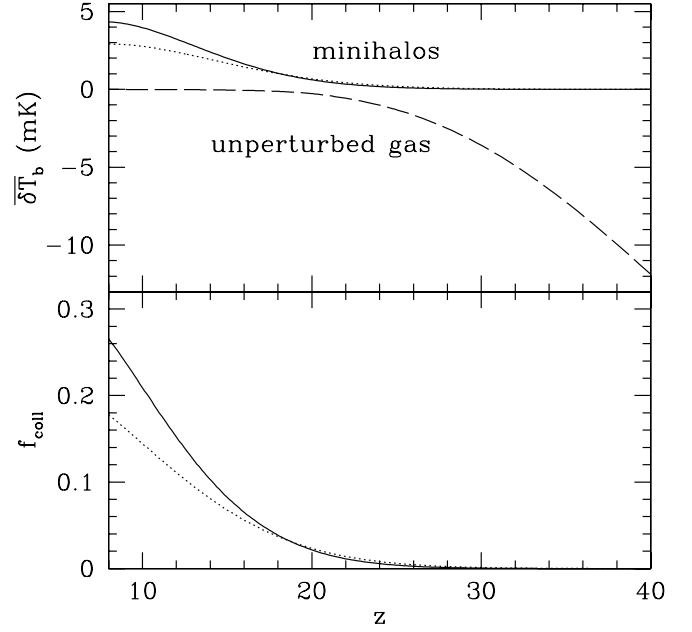

Fig. 1.—Analytical prediction for the mean 21 cm differential brightness temperature due to collisionally decoupled minihalos and an unperturbed IGM. Shown in the top panel are the results based on the Press-Schechter (*solid line*) and the Sheth-Tormen (*dotted line*) mass functions for halos and the contribution from IGM gas with cosmic mean density and temperature (*dashed line*). In the bottom panel, we show the minihalo collapsed fraction in the ΛCDM universe, again based on the Press-Schechter (*solid line*) and the Sheth-Tormen (*dotted line*) mass functions.

where

$$F(x) = \mathrm{dex}(3172.36 - 18037.3x + 43430.3x^2 - 57481.7x^3$$
$$+ 45150.0x^4 - 21042.1x^5 + 5388.50x^6 - 585.165x^7), \quad (15)$$

which is in absorption until collisional pumping becomes negligible at $z \simeq 20$ (Fig. 1; see also Bharadwaj & Ali 2004; Zygelman 2005).

2.1.2. *Perturbed Universe: Optically Thin Case*

Thermal Doppler broadening and Doppler shift by peculiar motions would drive ϕ to be broadened and shifted, causing overlap of line profiles. In such cases, the solution to equation (5), in general, is not given in a simple form as in equation (10). We show here, however, that the simple solution given by equation (13) also applies to the overlapped line profile case, as long as the optical depths, both infinitesimal and integrated, of gas in the simulation box are small. In such optically thin limits, equation (5) can be approximated as

$$T_b(\nu) = T_{\mathrm{CMB},0}(1-\tau_\nu) + \int_0^{\tau_\nu} d\tau_{\nu'}' \frac{T_S(z')}{1+z'}. \qquad (16)$$

The differential brightness temperature from a simulation box at z with a redshift spread $\Delta z\ (\ll z)$ and angle spread $\Delta\Omega$ is

$$\overline{\delta T}_b(\nu) \equiv \frac{\int d\nu\, d\Omega\, \delta T_b(\nu)}{\int d\nu\, d\Omega}, \qquad (17)$$

where the frequency and angle intervals of integration are set by the size of the box. As the angle integration is a simple sum of

different line-of-sight contributions that do not interfere with each other, we can first perform the line-of-sight average,

$$\overline{\delta T}_b(\nu)\big|_{\text{l.o.s.}} = \frac{\int_{\nu-\delta\nu/2}^{\nu+\delta\nu/2} d\nu \, \delta T_b(\nu)}{\int_{\nu-\delta\nu/2}^{\nu+\delta\nu/2} d\nu}, \tag{18}$$

and then integrate over angles. In equation (18) one can show that

$$\int_{\nu-\delta\nu/2}^{\nu+\delta\nu/2} d\nu = \frac{\nu_0}{(1+z)^2} \int_{z-\Delta z/2}^{z+\Delta z/2} dz', \tag{19}$$

and

$$\int_{\nu-\delta\nu/2}^{\nu+\delta\nu/2} d\nu \int_0^{\tau_\nu} d\tau'_{\nu'}$$

$$= \frac{c\nu_0^{-2}}{H(z)(1+z)^2} \int_{z-\Delta z/2}^{z+\Delta z/2} dz' \, \frac{3c^2 A_{10} n_{\text{H I}}(z') T_*}{32\pi T_S(z')}, \tag{20}$$

where we have used the fact that $\int_{-\infty}^{\infty} d\nu' \phi(\nu') = 1$ and have also assumed that the thermal broadening and the Doppler shift by peculiar motions are negligible compared to the width of the box: $(\Delta\nu')_{\text{thermal}} \ll \Delta\nu'_{\text{box}}$, $(\Delta\nu')_{\text{peculiar}} \ll \Delta\nu'_{\text{box}}$. Using equations (16), (19), and (20), we then obtain

$$\overline{\delta T}_b(\nu)\big|_{\text{l.o.s.}} = \frac{\int^{\Delta z} dz' [T_{S(z')}/(1+z') - T_{\text{CMB},0}] \tau(z')}{\int^{\Delta z} dz'}, \tag{21}$$

which is simply an averaged superposition of contributions of gas given by equation (13), along the line of sight.

We have shown, in this section, that the 21 cm differential brightness temperature $\overline{\delta T}_b(\nu)$ can be calculated by a simple average of individual contributions from gas at different locations in a simulation box, as long as optical depths are small (eq. [21]). Care needs to be taken, however, when gas achieves considerable optical depth. In § 2.1.3 we describe how one can calculate the signal from optically thick media, which are mostly located inside minihalos.

2.1.3. Perturbed Universe: Minihalos

Minihalos that start to emerge at $z \simeq 20$ have temperature and density high enough to produce a significant emission signal (ISFM02). As the optical depth through each minihalo is not negligible, the full radiative transfer equation (eq. [5]) should be solved through individual minihalos. Once individual halo contribution $\Delta\nu_{\text{eff}} \delta T_{b,\nu_0}$ is obtained for each given halo mass M, one can calculate $\overline{\delta T}_b$ from all the minihalos at redshift z by integrating over the halo mass function dn/dM:

$$\overline{\delta T}_b = \frac{c(1+z)^4}{\nu_0 H(z)} \int_{M_{\text{min}}}^{M_{\text{max}}} \Delta\nu_{\text{eff}} \delta T_{b,\nu_0} A \, \frac{dn}{dM} \, dM, \tag{22}$$

where $\Delta\nu_{\text{eff}}$, $\delta T_{b,\nu_0}$, and A refer to the parameters of the individual virialized halo, $\Delta\nu_{\text{eff}} = \Delta\nu'(1+z)^{-1} = (\nu_0'/c)(2kT/m)^{1/2}(1+z)^{-1}$, $\delta T_{b,\nu_0}$ is the face-averaged differential brightness temperature

at line center, and A is the projected surface area of the halo. ISFM02 based their calculation on the nonsingular, truncated isothermal sphere (TIS) model for CDM halos by Shapiro et al. (1999) and Iliev & Shapiro (2001), in which the halo density profile and virial temperature are fully specified by the halo mass and redshift, and the Press-Schechter (1974) mass function, which determines the number density of halos at a given redshift. The minimum minihalo mass M_{min} is set by the Jeans mass:

$$M_{\text{J}} = 5.7 \times 10^3 \left(\frac{\Omega_m h^2}{0.15}\right)^{-1/2} \left(\frac{\Omega_b h^2}{0.02}\right)^{-3/5} \left(\frac{1+z}{10}\right)^{3/2} M_\odot. \tag{23}$$

For M_{max}, ISFM02 used the mass for which the virial temperature is 10^4 K:

$$M_{\text{max}} = 3.95 \times 10^7 \left(\frac{\Omega_m h^2}{0.15}\right)^{-1/2} \left(\frac{1+z}{10}\right)^{-3/2} M_\odot. \tag{24}$$

The neutral baryonic fraction of halos with mass above M_{max} is uncertain, because hydrogen will be partially ionized due to collisions and photoionization by internal sources. Thus, the mass range from M_{min} to M_{max} naturally defines the mass range of minihalos that are fully neutral. Figure 1 depicts the predicted signals from unperturbed gas as well as from minihalos. We show results for both the Press-Schechter and the Sheth-Tormen mass functions (Sheth & Tormen 2002).

2.2. Numerical Simulations

We have run series of cosmological N-body and gasdynamic simulations to derive the effect of gravitational collapse and the hydrodynamics on the predicted 21 cm signal from high redshift. Our computational box has a comoving size of $0.5 \, h^{-1}$ Mpc, which is optimal for adequately resolving both the minihalos and the small-scale structure formation shocks. We used the code described in Ryu et al. (1993), which uses the particle mesh (PM) scheme for calculating the gravity evolution and an Eulerian total variation diminishing (TVD) scheme for hydrodynamics. We generated our initial conditions for the gas and dark matter distributions using the publicly available software COSMICS (Ma & Bertschinger 1995). The N-body/hydrocode uses an N^3 grid and $(N/2)^3$ dark matter particles. In order to check the convergence of our results we ran simulations at different spatial resolutions, with grid sizes 128^3, 256^3, 512^3, and 1024^3, which we denote by C1, C2, C3, and C4, respectively. We report our results in § 3 based on our highest resolution simulation C4 and discuss the convergence of the results in § 3.3.

After the decoupling of CMB photons from the baryonic gas, the IGM gas cools adiabatically due to cosmic expansion (eq. [12]). Equation (12) agrees, for instance, with the solution to the equation (1) in Bharadwaj & Ali (2004), which describes how T_{gas} evolves exactly. This temperature, $T_{\text{gas}}(z)$, was used in the simulation to set the minimum temperature of baryonic gas, to avoid negative temperatures.[6] If a gas cell is cooled below $T_{\text{gas}}(z)$, its temperature is set back to $T_{\text{gas}}(z)$. Such a temperature "floor"

---

[6] One should, in principle, use the locally varying minimum temperature. However, usage of a global minimum temperature is well justified as described in the text, and it is computationally cheaper than implementing a locally varying minimum temperature.

may overestimate the gas temperature of underdense regions, but because of their low density and temperature, y_c is small in these regions. This implies that the spin temperature T_S would be very close to T_{CMB}, and their contribution to δT_b would also be negligible, whether the kinetic temperature T_K is calculated accurately or not.

In addition to the total 21 cm signal from our simulations, $\overline{\delta T}_{b,\text{IGM}}$, we are also interested in the relative contribution of the virialized minihalos and the IGM to the total signal, the sum of which gives the total 21 cm signal, $\overline{\delta T}_{b,\text{tot}} = \overline{\delta T}_{b,\text{halo}} + \overline{\delta T}_{b,\text{IGM}}$. First, we calculate the total mean signal as a simple average over the simulation cells, $\overline{\delta T}_{b,\text{tot}} \equiv \sum_i \delta T_{b,i}/N^3$. The minihalo contribution is given by $\overline{\delta T}_{b,\text{halo}} \equiv \sum_i f_i \delta T_{b,i}/N^3$, where f_i is the fraction of the DM mass in a cell i that is part of a halo. The IGM contribution can then be obtained as

$$\overline{\delta T}_{b,\text{IGM}} = \overline{\delta T}_{b,\text{tot}} - \overline{\delta T}_{b,\text{halo}} = \sum_i (1 - f_i)\delta T_{b,i}/N^3. \quad (25)$$

In order to calculate the minihalo contribution to the total differential brightness temperature, $\overline{\delta T}_{b,\text{halo}}$, one needs to first identify the halos in the simulation volume. We identified the halos using a friends-of-friends (FOF) algorithm (Davis et al. 1985) with a linking length parameter of $b = 0.25$. The FOF algorithm applies to the dark matter N-body particles, rather than the gas in grid cells. Once this halo catalog is processed for each time slice of our N-body results, the baryonic component of each halo is identified for the grid cells of the hydrodynamics simulation that are contained within the volume of the halos in our FOF catalog. We do this as follows. First, the density in each cell contributed by each DM particle is determined by the triangular-shaped cloud assignment scheme. For each cell in which mass is contributed by the DM particles of a given halo, the gaseous baryonic component in that cell is assumed to contribute a fraction f_i of its mass given by the fraction of the total DM mass in that cell that is attributed to the halo DM particles. Accordingly, each cell i contributes an amount $f_i \delta T_{b,i}$ to the signal attributed to halo gas, while $(1 - f_i)\delta T_{b,i}$ is assumed to be the signal from the IGM outside of the halo, where $\delta T_{b,i}$ is calculated from the cell as a whole.

2.2.1. Semianalytical Calculation of the Halo Contribution

Our numerical simulations have sufficiently high resolution to find all halos in the computational box and the large-scale structure formation shocks, but not to resolve the internal structure of the minihalos themselves. However, as ISFM02 have shown, in order to obtain the correct 21 cm signal from minihalos one needs to do a full radiative transfer calculation through each individual minihalo density profile since, unlike the IGM gas, minihalos have a nonnegligible optical depth at the 21 cm line. Hence, we can refine our estimate of the minihalo contribution to the total 21 cm signal by combining our numerical halo catalogers with the semianalytical calculation of individual minihalo contribution as found by ISFM02. In their approach, as described in § 2.1.3, the gas density of each minihalo is assumed to follow a TIS profile (Iliev & Shapiro 2001), radiative transfer calculations are performed to determine the δT_b for different impact parameters, and, finally, the face-averaged δT_b is calculated (see ISFM02 for details). The halo mass function, dn/dM, is provided by the halo catalog we construct from the simulation. Each individual halo contribution, $\Delta\nu_{\text{eff}}\delta T_{b,\nu_0}A$, depends on its mass and redshift of formation (ISFM02). Once we calculate

$\Delta\nu_{\text{eff}}\delta T_{b,\nu_0}A$, we then obtain the halo contribution using equation (22).

3. RESULTS

3.1. *Numerical* 21 cm *Brightness Temperature from Minihalos versus IGM*

In this section, we describe the results from our simulations. In Figure 2 we show (unfiltered) maps of the differential brightness temperature obtained directly from our numerical data for our highest resolution simulation (C4), as described in § 2. We show the total signal, as well as the separate contributions from minihalos and IGM, derived as we described in § 2.2, at redshifts $z = 30$, 20, and 10. At $z = 30$, the earliest redshift shown (*top row*), most of the diffuse IGM gas is still in the quasi-linear regime and cold, thus largely in absorption against the CMB. At redshift $z = 20$ (*middle row*), the diffuse gas is still largely in absorption, while the (relatively few) halos that have already collapsed are strongly in emission. The combination of the two contributions creates a complex, patchy emission/absorption map, and absorption and emission partially cancel each other in the total mean signal. Finally, at $z = 10$ (*bottom row*), including its diffuse component, gas heated above T_{CMB} is widespread, leading to a net emission against the CMB. The bulk of this 21 cm emission comes from the high-density knots and filaments. Although both the halo and IGM contributions come from roughly the same regions, the minihalo emission is significantly more clustered, while the IGM emission is quite diffuse.

In Figure 3 we have plotted the volume-weighted probability distribution functions (PDFs) for the gas density $(1 + \delta)$ and the differential brightness temperature contributions δT_b as functions of each other. The PDFs for gas density show that, while the highest overdensities ($\delta \gtrsim 30$) are typically found inside minihalos and the lower overdensities ($\delta \lesssim 30$) and underdensities ($\delta \lesssim 0$) are typically associated with the IGM, there is some overlap of the distributions for these two components. A small fraction of the volume contains lower density minihalo gas and higher density IGM gas. However, the cumulative distributions show that these volumes hardly affect the total mean brightness temperature contributed by each component. Similarly, the PDFs for the brightness temperature show that, while the volume that contributes the highest brightness temperatures is predominantly inside minihalos and that which contributes the lower brightness temperatures is predominantly located in the IGM, there is, once again, some overlap of the PDFs. A small part of the IGM volume exhibits high brightness temperature, while a small part of the minihalo volume shows low brightness temperature. Once again, however, the cumulative distributions show that these regions hardly affect the total mean brightness temperatures contributed by each component.

In Figure 4 we quantify the relative contributions of the minihalos and diffuse IGM to the total mean 21 cm signal averaged over the whole computational box and their evolution. The evolution roughly follows the naive analytical estimates, as was shown in Figure 1. The total signal is deep in absorption, with $\delta T_b < -10$ mK at $z > 37$. The 21 cm signal is completely dominated by the IGM contribution at this stage. The absorption signal follows the analytical prediction for the unperturbed universe in § 2.1.1 well, since the density fluctuations are still small and the uniform density assumption is reasonably accurate. The absorption continually decreases as significant nonlinear structures start forming and portions of the gas became heated due to this structure formation. The net signal goes into emission after redshift
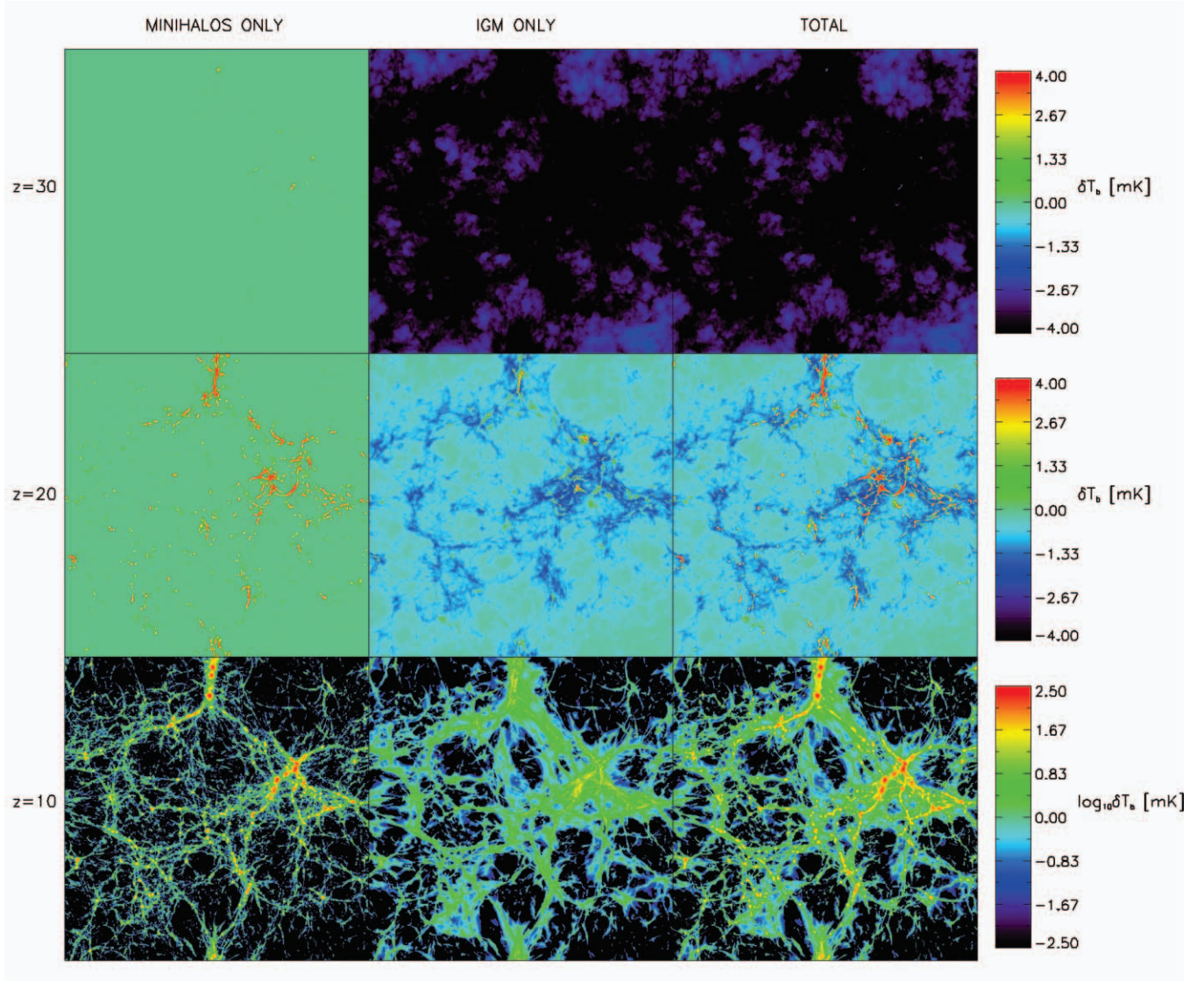
Fig. 2.—Map of the differential brightness temperature, δT_b (projected onto one surface of the box), for the redshifted 21 cm signal obtained from our highest resolution simulation, C4. Rows (*top to bottom*) show redshifts $z = 30$, 20, and 10, respectively. Columns (*left to right*) represent contributions from minihalos, the IGM, and the total signal, respectively. Note that the scale is linear in δT_b for the upper two rows of images, but logarithmic for the bottom row.

$z \sim 20$, reaching up to ~ 5 mK by $z \approx 8$. The emission signal at $z < 18$ is due to both collapsed halos and the clumpy, hot IGM gas. In terms of their relative contributions, the minihalos dominate over the diffuse IGM at all times when the overall signal is in emission, below $z = 18$. We find that the relative contributions to the total signal, $|\overline{\delta T}_{b,j}|/(|\overline{\delta T}_{b,\text{halo}}| + |\overline{\delta T}_{b,\text{IGM}}|)$, where j means either "halo" or "IGM," is nearly constant over two different redshift regimes: for $z > 20$, $|\overline{\delta T}_{b,\text{IGM}}|/(|\overline{\delta T}_{b,\text{halo}}| + |\overline{\delta T}_{b,\text{IGM}}|) \approx 1$, while for $z < 16$, $|\overline{\delta T}_{b,\text{halo}}|/(|\overline{\delta T}_{b,\text{halo}}| + |\overline{\delta T}_{b,\text{IGM}}|) \approx 0.7$. In the transition region, $16 \lesssim z \lesssim 20$, the relative contributions exhibit more complex behavior, approximately canceling each other out, resulting in a total signal that is close to zero.

3.2. Refined Estimate of the Simulated Minihalo 21 cm Signal

As we discussed in § 2.2.1, we can improve our purely numerical estimate of the minihalo 21 cm signal by replacing each halo's flux with the value obtained by detailed radiative transfer calculations. We obtain the total minihalo signal from equation (22), with the theoretical mass function dn/dM replaced by the actual, numerical halo catalog obtained from our simulations,

and the individual minihalo contributions, $\Delta \nu_{\text{eff}} \delta T_{b,\nu_0} A$, calculated by modeling each halo as a TIS.

We find that the resulting 21 cm signal from halos is stronger than the "raw" numerical signal obtained directly from the simulated halos and dominates the overall emission signal even more (Fig. 5). This is despite the fact that our consideration of the more centrally concentrated analytical density profiles increases the optical depth of each halo. We attribute this nonintuitive behavior to the fact that the density profiles of the minihalos found in our simulations are not fully resolved. By modeling the halo density profiles in detail, the local density inside halos is boosted, which significantly increases the coupling constant y_c, which, in turn, increases the total emission signal, even though the optical depth through each halo also increases simultaneously. Note that we use the same population of halos for both estimates, and only the internal halo properties are modified.

In Figure 6 we show the total minihalo collapsed fraction obtained from the simulations compared to that from the theoretical Press-Schechter (PS) and Sheth-Tormen (ST) halo mass functions. We also show the minihalo contribution to the total
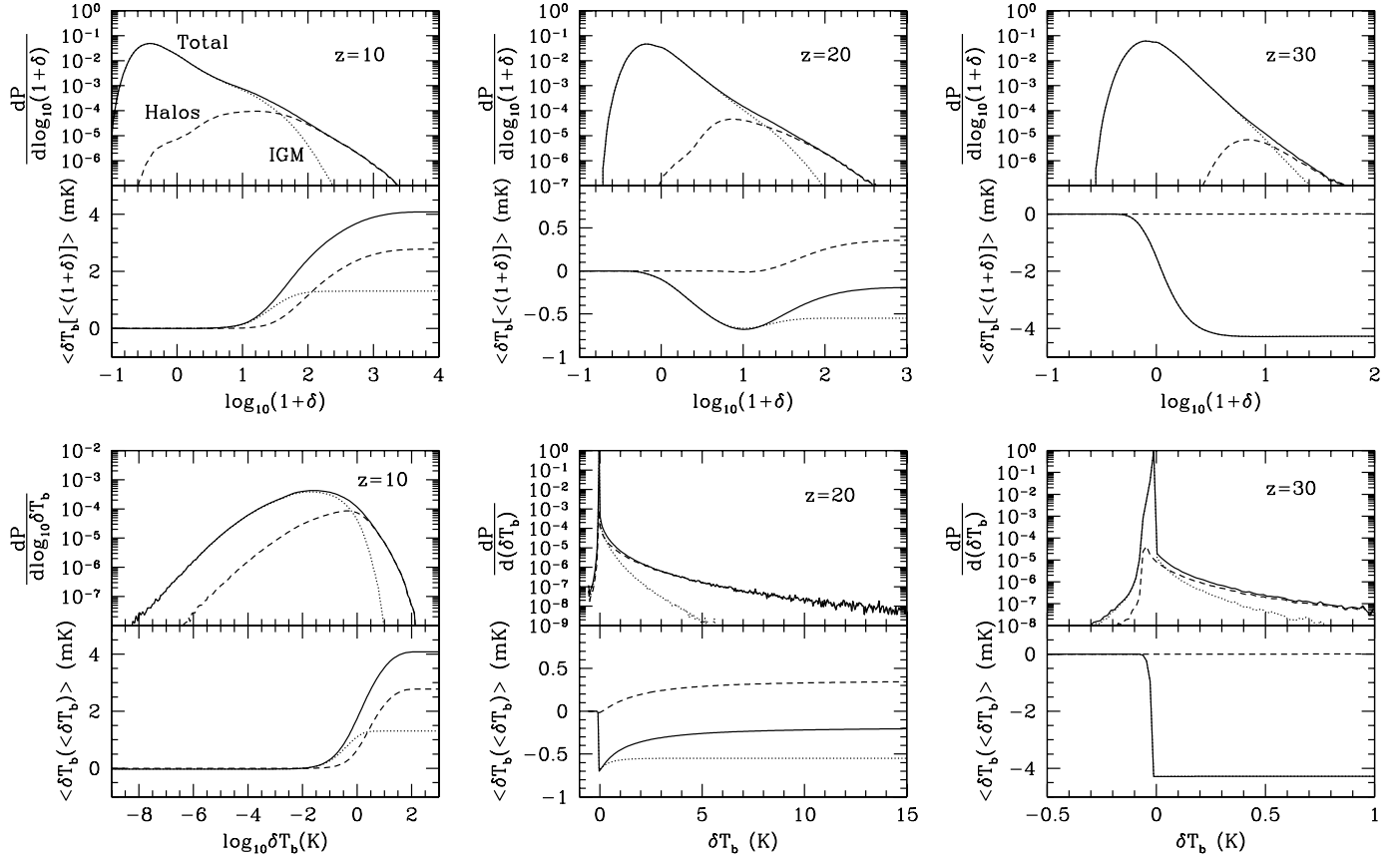
FIG. 3.—Volume-weighted probability distribution functions (PDFs) of gas density $(1 + \delta)$ and differential brightness temperature (δT_b) for C4 vs. $(1 + \delta)$ and δT_b, respectively, for the total gas (*solid lines*), MH gas (*dashed lines*), and IGM gas (*dotted lines*). Also shown are the cumulative differential brightness temperatures, i.e., $\langle \delta T_b (<[1 + \delta]) \rangle$ and $\langle \delta T_b (<\delta T_b) \rangle$. The top and bottom panels (*left to right*) correspond to $z = 10$, 20, and 30, respectively.
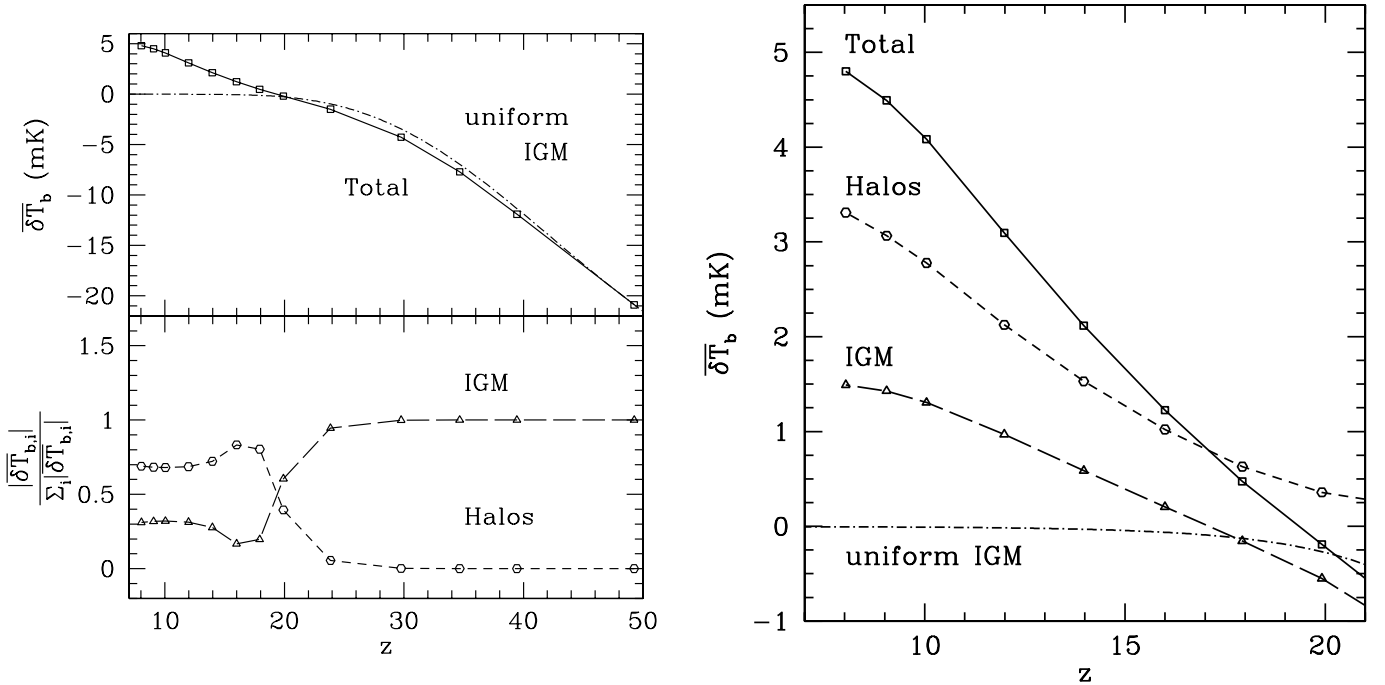
FIG. 4.—Evolution of mean differential brightness temperature, $\overline{\delta T_b}$, of 21 cm background. *Left:* Evolution of the total 21 cm signal vs. redshift. All data points are directly calculated from our highest resolution (C4) simulation box, with the assumption that optical depth is negligible throughout the box. *Right:* $\overline{\delta T_b}$ vs. redshift below $z = 20$. The contributions from minihalos (*circles*), the IGM (*triangles*), and the total (*squares*) are plotted, as labeled. For comparison, the result for the unperturbed IGM is also plotted (*dash-dotted curves*).
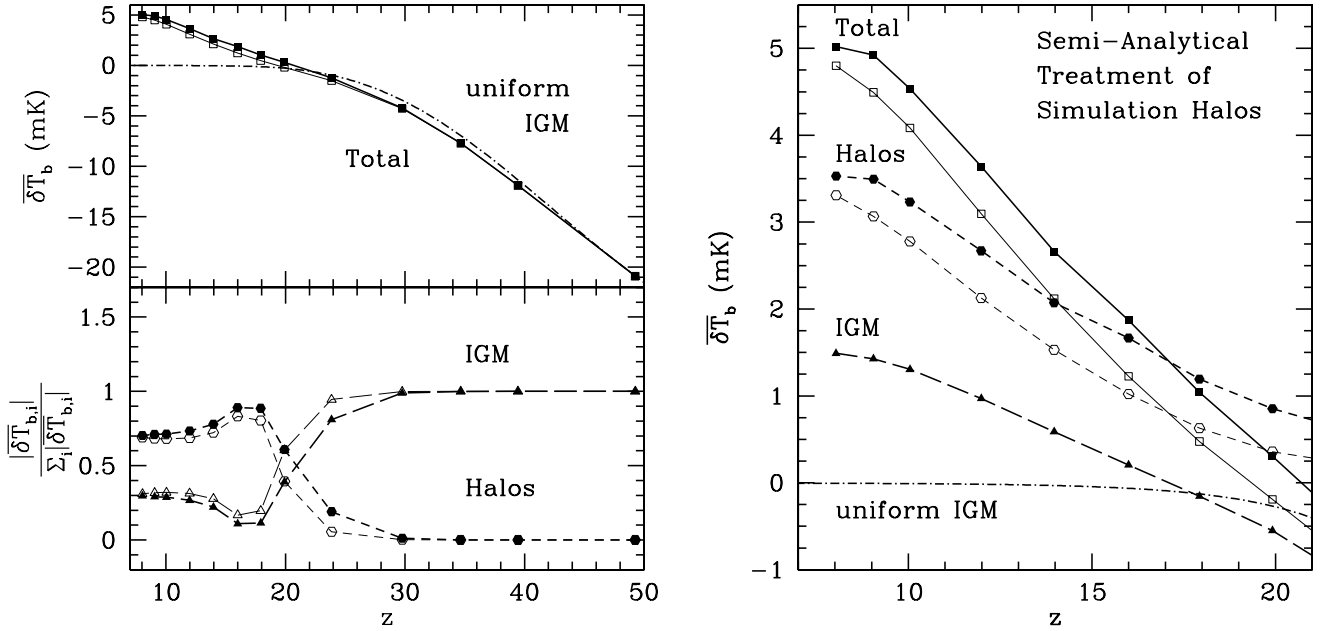
Fig. 5.—Semianalytical minihalo signal vs. IGM signal. The 21 cm flux from each halo in the simulation is found by modeling the internal structure and 21 cm line transfer through individual halos as described by ISFM02 (§ 2.2.1) to calculate the halo 21 cm signal from each halo more accurately. Notation is the same as in Fig. 4. The semianalytical 21 cm minihalo emission is higher than the raw simulated minihalo signal in Fig. 4. The IGM signal remains the same. The raw minihalo and total signals plotted in Fig. 4 (*thin lines and open symbols*) are also shown for comparison.

differential brightness temperature signal. We see that the collapsed fraction in minihalos in our simulation roughly agrees with the analytical predictions, mostly lying between PS and ST results. On the other hand, the minihalo contribution to the total 21 cm background obtained directly from the simulation is below the theoretical predictions based on either PS or ST mass functions.
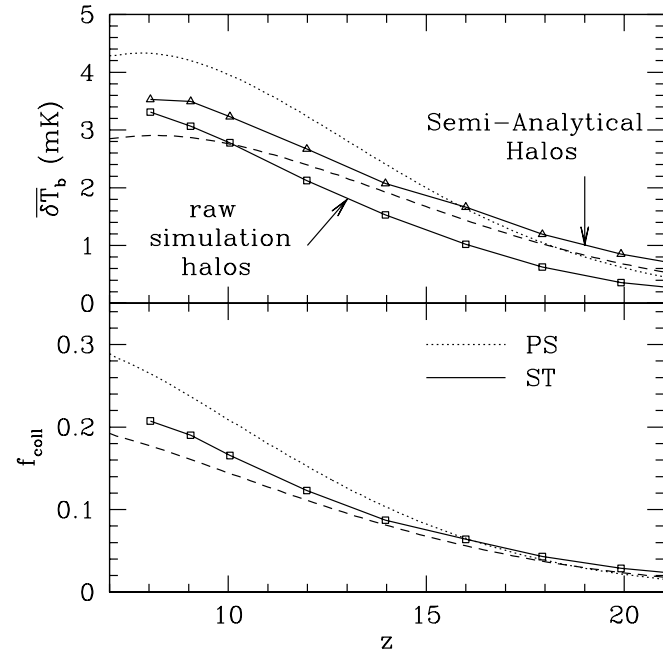

Fig. 6.—Comparison of analytical and numerical minihalo results. *Top*: Differential brightness temperature of the 21 cm signal from minihalos for semianalytical model (*dotted line*: with Press-Schechter mass function; *dashed line*: with Sheth-Tormen mass function), simulation C4 numerical result (*squares*), and semianalytical calculation (§ 2.2.1) based on simulation C4 mass function (*triangles*). *Bottom*: Minihalo collapse fraction from simulation C4 (*squares*) and analytical mass functions (line types same as top panel).

The agreement is restored, however, when we replace each minihalo contribution to the total flux by its analytically modeled value. This, once again, underscores the importance of resolving the internal halo structure for correct predictions of their 21 cm emission.

3.3. Numerical Convergence

We now compare cases C1, C2, C3, and C4 to check the robustness of our results with respect to numerical convergence. In Figure 7 we show the differential brightness temperature signals for our three lower resolution simulations, C1, C2, and C3, in terms of the signal obtained from our highest resolution simulation, C4. We show the total signal, as well as each separate contribution, from either the halos or the IGM gas. At $z > 20$ most of the gas density fluctuations are still linear, and a change in the resolution barely affects the results. Thus, a modest-resolution simulation, or even the analytical estimate for an unperturbed IGM, suffices to obtain reliable results. In contrast, at lower redshifts ($z < 20$) the results depend strongly on the resolution. The low-resolution simulations C1 and C2 underestimate the resulting 21 cm signal significantly, by factors of up to a few. The results from these simulations improve somewhat at lower redshifts, below $z = 10$, but results are still below the ones from C4 by $\sim$30%–50% and $\sim$20% for simulations C1 and C2, respectively. This is true for either the minihalo, IGM, or the total signal. The results from our medium-resolution simulation C3, on the other hand, are much closer to the ones from the high-resolution simulation C4, with the two generally agreeing to better than 10%. This indicates convergence of our results to within a few percent for simulation C4. Such behavior could be naïvely expected, since at $z < 20$ nonlinear structures, both collapsed halos and mildly nonlinear, shocked IGM gas, form in abundance at the scales we are investigating, and thus high resolution is required to resolve these properly, as our simulations confirm.

The relative contributions of the minihalo and the IGM signals, on the other hand, show a more robust convergence (Fig. 8).
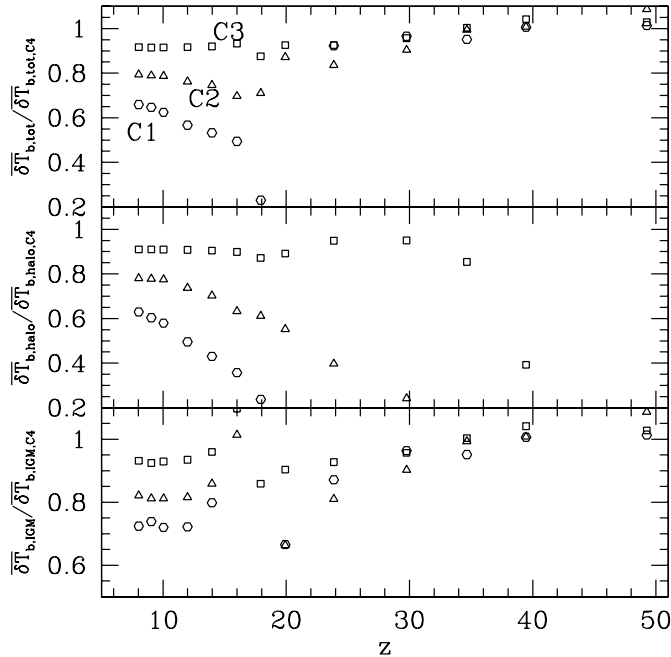
Fig. 7.—Numerical resolution convergence results. Mean differential brightness temperature signals for simulations C1 (*squares*), C2 (*triangles*), and C3 (*circles*) in units of the corresponding signal obtained from our highest resolution simulation, C4. Shown are 21 cm signals from the total (*top*), halos only (*middle*), and IGM only (*bottom*).
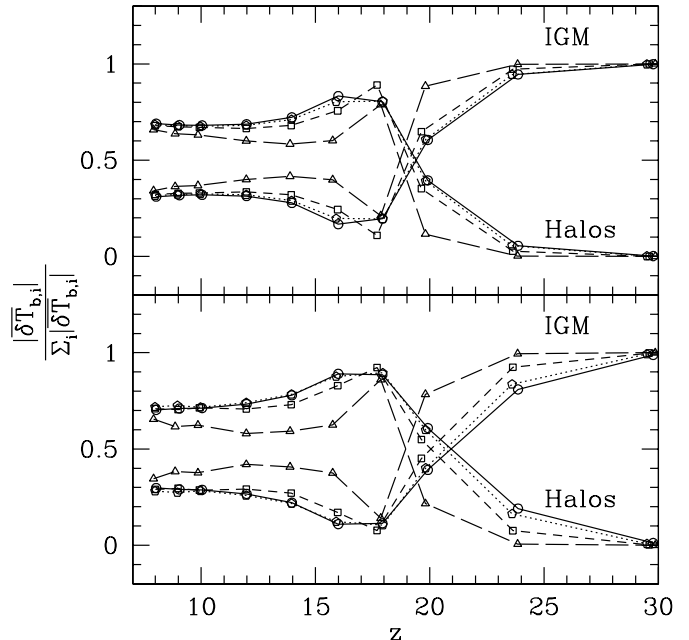

Fig. 8.—Numerical resolution convergence results. Relative contributions of minihalos and diffuse IGM gas to the total 21 cm background. The top panel shows the results obtained directly from simulations (C1: *triangles, long-dashed lines*; C2: *squares, short-dashed lines*; C3: *pentagons, dotted lines*; C4: *circles, solid lines*). The bottom panel shows the results that were semianalytically refined (§ 2.2.1; point and line types same as top panel).

In all cases of different resolutions, we find that the minihalo signal dominates the IGM signal at $z < 20$, while the IGM signal dominates the minihalo signal at $z > 20$. For the purely numerical result, the relative contribution of minihalos to the emission signal is about 70% at $z < 15$, peaks to 100% at $z \approx 18$, and drops to 50% at $z \approx 20$. The exact value of the transition redshift varies slightly with resolution. For $z < 14$, minihalos contribute ~70% of the emission signal. For the case of semianalytical calculation of the minihalo contribution based on the simulated halo catalogs, the relative contribution to the emission signal is slightly higher, ~75%.

4. CONCLUSIONS

We have run a set of cosmological N-body and hydrodynamic simulations of the evolution of dark matter and baryonic gas at high redshift ($6 < z < 100$). With the assumption that radiative feedback effects from the first light sources are negligible, we calculated the mean differential brightness temperature of the redshifted 21 cm background at each redshift. The mean global signal is in absorption against the CMB above $z \sim 20$ and in overall emission below $z \sim 18$. At $z > 20$, the density fluctuations of the IGM gas are largely linear, and their absorption signal is well approximated by the one that results from assuming uniform gas at the mean adiabatically cooled IGM temperature. At $z < 20$, nonlinear structures become common, both minihalos and clumpy, hot, mildly nonlinear IGM, resulting in an overall emission at 21 cm with differential brightness temperature of order a few millikelvins.

By identifying the halos in our simulations, we were able to separate and compare the relative contributions of the halos and the IGM gas to the total signal. We find that the emission from minihalos dominates over that from the IGM outside minihalos, for $z \lesssim 20$. In particular, the emission from minihalos contributes about 70%–75% of the total emission signal at $z < 17$, peaking at 100% at $z \approx 18$, and balancing the absorption by the IGM gas

at $z \approx 20$. In contrast, the absorption by cold IGM gas dominates the total signal for $z > 20$.

These results appear to contradict the suggestion by Furlanetto & Loeb (2004) that the 21 cm emission signal would be dominated by the contribution of shocked gas in the diffuse IGM. They used the Press-Schechter formalism to estimate the fraction of the IGM outside of minihalos, which is shock heated, by adopting a spherical infall model for the growth of density fluctuations and assuming that all gas inside the turnaround radius is shock heated. This method is apparently not accurate enough to describe the filamentary nature of structure formation in the IGM.

On the other hand, our results are consistent with the analytical estimates of the mean 21 cm emission signal from minihalos by ISFM02. This indicates that the statistical prediction of the collapsed and virialized regions identified as minihalos by the Press-Schechter formalism (or its refinement in terms of the Sheth-Tormen formula), with virial temperatures $T < 10^4$ K, with halos characterized individually by the TIS model, is a reasonably good approximation for the mean 21 cm signal for minihalos at all redshifts and a good estimator even for the total mean signal including both minihalos and the diffuse IGM at $z \lesssim 20$. This encourages us to believe that the angular and spectral fluctuations in the 21 cm background predicted by ISFM02 based on that model will also be borne out by future simulations involving a much larger volume than was simulated here. The current simulation volume is too small to be used to calculate the fluctuations in the 21 cm background, because current plans for radio surveys to measure this background involve beams that will sample much larger angular scales (>arcminutes) than are subtended by our current box [$\Delta\theta_{box} \sim 0\farcm2(1 + z)_{20}^{0.2}$, where $(1 + z)_{z'} = (1 + z)/(1 + z')$] and bandwidths ($\sim$MHz) that are too large to resolve the depth of our simulation box in redshift space (i.e., $\Delta\nu_{box} \sim 40$ kHz$(1 + z)_{10}^{-1/2}[L/(0.5\ h^{-1}\ \text{Mpc})]$). According to ISFM02 and Iliev et al. (2003), the fluctuations in the

21 cm background from minihalos are significantly enhanced by the fact that minihalos are biased relative to the total matter density fluctuations. A larger simulation volume than ours will also be necessary to sample this minihalo bias in a statistically meaningful way. This bias is likely to affect the minihalo contribution to the 21 cm background fluctuations substantially more than it does the diffuse IGM contribution, thereby boosting the relative importance of minihalos over the IGM even above the ratio of their contributions to the mean signal.

We have considered the limit in which only collisional pumping is available to decouple the spin temperature from that of the CMB, and sources of radiative pumping have not yet emerged to compete with this process. The possibility exists, however, that an X-ray background built up as sources formed inside some halos, which heated the IGM while only partially ionizing it (e.g., Oh & Haiman 2003). This heating might have boosted the kinetic temperature of the IGM and enhanced the effect of collisional pumping there (e.g., Chen & Miralda-Escudé 2004).[7] Such X-ray heating would also have raised the minimum mass of minihalos that formed thereafter, filled with their fair share of neutral H atoms. When stellar sources began to form and build up the UV background at energies below the Lyman limit of hydrogen, Lyα pumping could then have radiatively coupled T_S to T_K, as well. The same sources presumably emitted UV radiation above the H Lyman limit, too, which ionized both the IGM and the minihalos within the H II regions surrounding these sources (e.g., Shapiro et al. 2004; Iliev et al. 2005a, 2005b). Such H II regions would have created holes in the 21 cm background, which then originated only in the remaining neutral regions. Minihalos could have lost the neutral hydrogen gas responsible for their 21 cm emission, not only by "outside-in" photoionization by an external source, but also by "inside-out" photoionization by internal Population III star formation (e.g., Kitayama et al. 2004; Alvarez et al. 2006). The H$_2$ formation required for minihalos to form stars, however, is likely to have been suppressed easily by photodissociation in the Lyman-Warner bands by the background of UV radiation created by the very first minihalos that formed stars, when the ionizing radiation background was still much too low to cause reionization (Haiman et al. 2000). In that case, most minihalos would have remained intact until they were ionized from without. In the future, we plan to improve on the current calculation by incorporating this more complicated physics. We also intend to run simulations with larger simulation boxes. This would allow us to predict the 21 cm fluctuation signal (e.g., ISFM02) and determine whether the relative contribution of minihalos to the total signal, which we find to be about 70%–75% at $z \lesssim 20$ for the mean signal, varies as the mean signal fluctuates.

---

[7] Recently, Kuhlen et al. (2006) considered the X-rays emitted by an early miniquasar, finding that such an X-ray source can heat the IGM to as much as a few thousand degrees kelvin without ionizing it. This boosts the 21 cm signal from collisionally decoupled gas in the diffuse IGM significantly. Their calculations neglect the ionizing UV radiation that might also be released by the miniquasar and its stellar progenitor, as well as the Lyα pumping they might contribute.

REFERENCES

Ahn, K., Shapiro, P. R., Alvarez, M. A., Iliev, I. T., Martel, H., & Ryu, D. 2006, NewA Rev., 50, 179
Allison, A. C., & Dalgarno, A. 1969, ApJ, 158, 423
Alvarez, M. A., Bromm, V., & Shapiro, P. R. 2006, ApJ, 639, 621
Barkana, R., & Loeb, A. 2004, ApJ, 609, 474
Bharadwaj, S., & Ali, S. S. 2004, MNRAS, 352, 142
Carilli, C. L., Gnedin, N. Y., & Owen, F. 2002, ApJ, 577, 22
Chen, X., & Miralda-Escudé, J. 2004, ApJ, 602, 1
Ciardi, B., & Madau, P. 2003, ApJ, 596, 1
Davis, M., Efstathiou, G., Frenk, C. S., & White, S. D. M. 1985, ApJ, 292, 371
Field, G. B. 1959, ApJ, 129, 536
Furlanetto, S. R., & Loeb, A. 2002, ApJ, 579, 1
———. 2004, ApJ, 611, 642
Furlanetto, S. R., Sokasian, A., & Hernquist, L. 2004, MNRAS, 347, 187
Gnedin, N. Y., & Shaver, P. A. 2004, ApJ, 608, 611
Haiman, Z., Abel, T., & Rees, M. J. 2000, ApJ, 534, 11
Iliev, I. T., Scannapieco, E., Martel, H., & Shapiro, P. R. 2003, MNRAS, 341, 81
Iliev, I. T., Scannapieco, E., & Shapiro, P. R. 2005a, ApJ, 624, 491
Iliev, I. T., & Shapiro, P. R. 2001, MNRAS, 325, 468
Iliev, I. T., Shapiro, P. R., Ferrara, A., & Martel, H. 2002, ApJ, 572, L123 (ISFM02)
Iliev, I. T., Shapiro, P. R., & Raga, A. C. 2005b, MNRAS, 361, 405
Kitayama, T., Yoshida, N., Susa, H., & Umemura, M. 2004, ApJ, 613, 631
Kuhlen, M., Madau, P., & Montgomery, R. 2006, ApJ, 637, L1
Ma, C.-P., & Bertschinger, E. 1995, ApJ, 455, 7
Madau, P., Meiksin, A., & Rees, M. J. 1997, ApJ, 475, 429
Martel, H., Shapiro, P. R., Iliev, I. T., Scannapieco, E., & Ferrara, A. 2003, in AIP Conf. Proc. 666, The Emergence of Cosmic Structure, ed. S. S. Holt & C. S. Reynolds (Melville: AIP), 85
Oh, S. P., & Haiman, Z. 2003, MNRAS, 346, 456
Press, W. H., & Schechter, P. 1974, ApJ, 187, 425
Purcell, E. M., & Field, G. B. 1956, ApJ, 124, 542
Ryu, D., Ostriker, J. P., Kang, H., & Cen, R. 1993, ApJ, 414, 1
Scott, D., & Rees, M. J. 1990, MNRAS, 247, 510
Shapiro, P. R., Iliev, I. T., & Raga, A. C. 1999, MNRAS, 307, 203
———. 2004, MNRAS, 348, 753
Shaver, P. A., Windhorst, R. A., Madau, P., & de Bruyn, A. G. 1999, A&A, 345, 380
Sheth, R. K., & Tormen, G. 2002, MNRAS, 329, 61
Subramanian, K., & Padmanabhan, T. 1993, MNRAS, 265, 101
Tozzi, P., Madau, P., Meiksin, A., & Rees, M. J. 2000, ApJ, 528, 597
Wouthuysen, S. A. 1952, AJ, 57R, 31
Zaldarriaga, M., Furlanetto, S. R., & Hernquist, L. 2004, ApJ, 608, 622
Zygelman, B. 2005, ApJ, 622, 1356